Systematic exploration of direct solar absorption potential to enhance direct contact membrane distillation

Desalination 606 (2025) 118740

Contents lists available at ScienceDirect

Desalination

journal homepage: www.elsevier.com/locate/desal

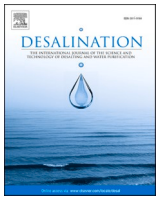

Systematic exploration of direct solar absorption potential to enhance direct contact membrane distillation

Roberto Raffaele Meo [a], Lorenzo Craveri [b], Erica Bertozzi [b], Marco Malaguti [b], Alberto Tiraferri [b,c], Matteo Morciano [a,c,*], Matteo Fasano [a,c,*]

[a] Department of Energy, Politecnico di Torino, Corso Duca degli Abruzzi 24, 10129 Torino, Italy
[b] Department of Environment, Land and Infrastructure Engineering, Politecnico di Torino, Corso Duca degli Abruzzi 24, Torino, 10129, Italy
[c] Clean Water Center, Politecnico di Torino, Corso Duca degli Abruzzi 24, 10129 Torino, Italy

HIGHLIGHTS

- Hybrid bulk and direct solar heating optimize DCMD desalination performance.
- Systematic parameter evaluation unlocks optimal performance in solar-enhanced MD.
- Longer modules, low feed temperature and velocity maximize solar-enhanced MD flux.
- Direct solar absorption reduces temperature polarization and enhances efficiency.
- Optimizing flow and heat transfer improves water flux by over 200% in MD.

ARTICLE INFO

Dataset link: Dataset for "Systematic exploration of direct solar absorption potential to enhance direct contact membrane distillation" (1.0) (Original data)

Keywords:
Membrane distillation
Desalination
Solar energy
Heat and mass transfer
Sustainability

ABSTRACT

Increasing concerns about global freshwater scarcity and the growing demand for renewable energy are stimulating the exploration of innovative technological solutions for sustainable water management. Thanks to an experimentally validated model, here we systematically assess the effectiveness of distributed solar heat in enhancing the productivity of direct contact membrane distillation (DCMD) for seawater desalination. The proposed study investigates the impact of various configurations and operating parameters, analyzing more than 1000 cases, focusing on optimizing heat and mass transfer, hence water flux, in counter-current and co-current channel designs. Our findings indicate that integrating solar heat can significantly improve DCMD performance, with productivity enhancements potentially exceeding 200%, especially at low cross-flow rates, by alleviating temperature polarization and enhancing vapor flux. The detailed analysis further reveals that the counter-current configuration consistently outperforms the co-current design under optimal conditions, achieving higher water fluxes and reduced polarization effects. Moreover, sensitivity studies underscore that fine-tuning channel dimensions and flow parameters is critical for maximizing energy efficiency and ensuring robust desalination performance. The results highlight the potential of solar-powered MD systems to provide sustainable and cost-effective freshwater solutions, particularly for off-grid and remote areas. By optimizing solar heat utilization and MD configurations, this study advances both theoretical understanding and practical applications in water desalination, promoting energy efficiency, operational cost reduction, and environmental sustainability.

1. Introduction

The availability of clean water and the development of renewable energy resources rank among the current world's most pressing challenges. Global water consumption is projected to increase by 55% by 2050 [1]. By then, more than 40% of people worldwide is expected to live in areas experiencing water scarcity, while, currently, 768 million people lack access to water suitable for human consumption [1]. Seawater desalination has become a viable solution to water shortages in regions with limited natural freshwater resources [2]. However, traditional desalination technologies are mostly powered by fossil fuels, which are costly and linked to climate change [3–5].

* Corresponding authors at: Department of Energy, Politecnico di Torino, Corso Duca degli Abruzzi 24, 10129 Torino, Italy.
E-mail addresses: matteo.morciano@polito.it (M. Morciano), matteo.fasano@polito.it (M. Fasano).

https://doi.org/10.1016/j.desal.2025.118740
Received 20 December 2024; Received in revised form 20 February 2025; Accepted 22 February 2025
Available online 28 February 2025

Developing more sustainable and innovative desalination technologies is a promising strategy to address this problem [6–8]. Thermal-driven membrane distillation (MD) is particularly promising due to its unique advantages [9]. Operating at lower temperatures compared to conventional thermal desalination processes, MD reduces the energy consumption since it allows to recover and exploit waste heat [10,11]. Differences in temperature between fluid streams are the main requirement for the functioning of MD, and these can be easily supplied by solar collectors. These collectors are simple to construct, technologically straightforward, and require minimal maintenance, except for regular cleaning. These features make MD a highly promising desalination technology, especially for feed solutions characterized by high salinity [12,13].

Despite these advantages, MD systems have seen limited adoption in the desalination industry, mainly due to their high costs and low water production rates compared to large-scale conventional desalination systems [14,15]. A major challenge in MD technology is achieving a uniform distribution of heat within the feed channel. Uneven heat distribution leads to temperature polarizations and gradients [16,17], where certain regions of the membrane receive less heat than others, impairing vapor transport and reducing the overall performance of the process. The presence of the temperature boundary layer causes the membrane surface temperature to be lower than that of the bulk liquid on the feed side, decreasing the vapor pressure gradient driving the mass transport [18,19]. Therefore, substantial thermal energy is lost to the permeate side, leading to lower energy utilization efficiency and suboptimal desalination performance [20]. Overcoming the challenge of uneven heat distribution in MD requires advanced module design and engineering solutions to ensure consistent heat distribution across the membrane surface, thereby optimizing the efficiency and longevity of the MD system.

Another key challenge in MD is achieving high energy efficiency, as the process requires a consistent and cost-effective heat source to maintain the temperature gradient required for vapor transport. Solar energy offers a promising sustainable option for desalination due to its accessibility and low maintenance demands [4]. In the context of MD, low-temperature solar heat can be strategically utilized to enhance process efficiency [21]. The integration of solar thermal energy involves distributing heat along the feedwater channel within the system. Various solar systems have been proposed to power MD indirectly, such as flat plate (FPSC) [22–25], evacuated tube (ETSC) [26–28] solar collectors, solar concentrators [29,30], parabolic trough collectors [31], and solar ponds [32]. Among these, FPSC and ETSC are commonly used for driving MD [33].

The direct use of solar energy in MD systems has received attention over the past decade, particularly for small-scale applications, including providing freshwater in remote off-grid areas [34,35], treating wastewater and water produced from oil extraction activities [36], supplying water and heating for residential buildings [37], producing water and cooling effects for photovoltaic solar panels [38], and producing water for agricultural use [39]. A novel solar MD (SMD) process has been developed to enhance desalination performance. Unlike the traditional MD process that relies on solar energy to heat seawater externally, the SMD process deploys a hydrophobic membrane with high photothermal conversion efficiency, enabling localized heating on the feed side. By concentrating heat near the membrane, the SMD process alleviates temperature polarization effects, improving energy utilization efficiency and seawater desalination performance [40]. However, a systematic investigation of the optimal configuration and operating conditions of MD modules and systems that exploit direct solar use is currently missing [41].

The primary objective of this work is to systematically evaluate the efficacy of distributed solar heat absorption on the feedwater side of the module to enhance the performance of direct contact membrane distillation (DCMD). This research focuses on analyzing how different configurations and operational parameters, such as flow velocity and temperature gradients, influence the overall productivity and efficiency of the MD process. Specifically, it aims to optimize the design of the feed channel to maximize heat transfer and productivity, evaluating the benefits of counter-current versus co-current configurations.

This research has the potential to improve energy efficiency, reduce costs, and promote sustainability in water desalination. By optimizing direct solar heat use and DCMD configurations, it offers more sustainable and cost-effective solutions for freshwater production from saline sources. The findings also underscore the role of direct solar absorption in reducing polarization effects, especially near the outlet section of the module. Overall, this work contributes valuable knowledge with practical implications for the design of efficient and sustainable desalination systems.

2. Theoretical background and methods

Here, the theoretical background and the methodological approaches used to study the DCMD process enhanced with direct solar absorption under different configurations and operating conditions are discussed. In Fig. 1, a schematic representation of the DCMD module is reported. In detail, the diagram on the left illustrates the counter-current configuration, in which the hot feed aqueous solution (see red arrow) flows from left to right in the upper channel, while the cold permeate aqueous solution (see blue arrow) flows in the opposite direction in the lower channel. The diagram on the right depicts the co-current configuration, in which both the hot feed and permeate cold aqueous solutions flow in the same direction. The dashed line represents the membrane that separates the two solutions. The length of the module (L), the height of the feed and permeate channels (δ) and the inlet flow velocity and temperature of the feed aqueous solution ($v_{feed,inlet}$ and $T_{feed,inlet}$, respectively) are also indicated. In addition, yellow arrows above the upper channel indicate the presence of any distributed solar radiation (q_{sun}) directly absorbed on the feed side. All these operating parameters are varied to study different scenarios. In the permeate channel, the inlet velocity ($v_{permeate,inlet}$) is assumed to be equal to the feed inlet velocity ($v_{feed,inlet}$). For simplicity, we refer to both velocities as v_{inlet}. This assumption is based on the fact that maximum productivity is achieved when the thermal inertias of the two channels are balanced. Any imbalance in thermal inertia leads to suboptimal temperature profiles at the membrane, ultimately reducing overall performance [16,42]. Supplementary Note 1 provides numerical results demonstrating that peak productivity occurs under these conditions, analyzing the effect of varying the permeate-to-feed velocity ratio and channel height ratio. These results confirm that deviations from equal inlet velocities and equal channel heights lead to a decline in productivity, reinforcing that this assumption ensures optimal thermal coupling and maximized performance. Furthermore, it is assumed that the temperature of the permeate at the inlet ($T_{permeate,inlet}$) is equal to the ambient temperature.

Therefore, heat and mass transfer equations are first formulated in detail for both channels. The formulation includes species transport, latent heat transfer resulting from phase change, and heat conduction across the hydrophobic and insulating membrane, and thus quantifies influences arising from the formation of temperature and concentration boundary layers at the interfaces between the aqueous solutions (both feed and permeate) and the membrane. It is worth noting that, while spacers are commonly used in practical applications, they are not included in the present model to maintain simplicity and focus on the overall module behavior. This choice allows for a more fundamental assessment of the effects of distributed heating on system performance. Moreover, neglecting spacers represents a conservative assumption, as their presence would enhance mixing and reduce polarization effects. Following this theoretical overview, the study discusses the specific methodologies employed, including the modeling frameworks and experimental setups used to simulate and validate the MD process.

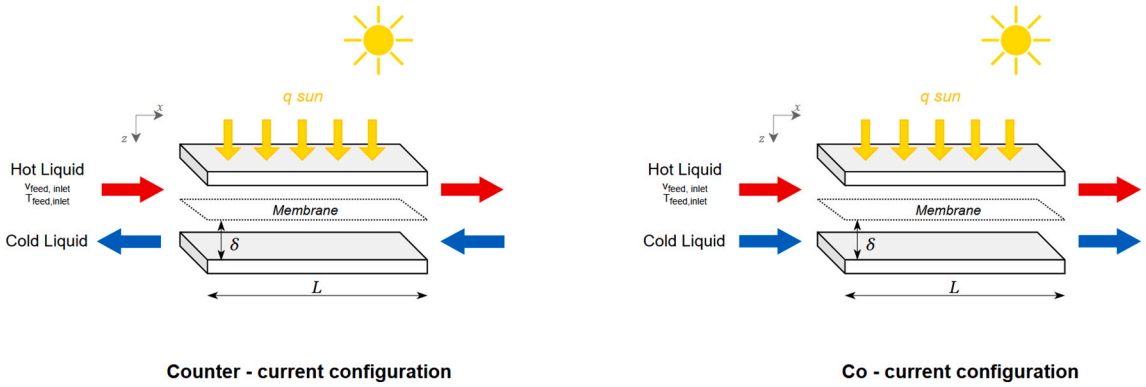

Fig. 1. Schematic of the DCMD module in counter-current and co-current configurations. The diagram on the left-hand side illustrates the counter-current configuration setup, where the hot liquid (red arrow) flows from left to right in the upper channel, while the cold liquid (blue arrow) flows in the opposite direction in the lower channel. The diagram on the right-hand side depicts the co-current configuration where both the hot and cold liquids flow in the same direction. The dashed line represents the membrane separating the two channels, while solid horizontal lines at the top and bottom delimit the channels. Yellow arrows above the upper channel indicate distributed solar radiation (q_{sun}). The module length (L), the channel height (δ), the inlet feed flow velocity ($v_{feed,inlet}$), and inlet feed temperature ($T_{feed,inlet}$) are also indicated. These parameters are degrees of freedom. Instead, the inlet velocity of the permeate stream is assumed to be equal to the feed inlet velocity. Additionally, the permeate inlet temperature is assumed to be equal to the ambient temperature.

2.1. Advection-diffusion equations for heat and mass transfer

The partial differential equations that describe the thermal dynamics within a fixed control volume Ω (i.e. the simulated DCMD module), where the boundary $\partial\Omega$ remains constant over time, are developed using the Eulerian framework. Specifically, applying the first law of thermodynamics to the control volume yields the following expression [43]:

$$\frac{d}{dt}\int_{\Omega}\rho c_p T\, d\Omega = -\oint_{\partial\Omega}\sum_i \Phi_i\cdot\mathbf{n}\, d\Sigma \tag{1}$$

where, ρ, c_p, and T denote the density, specific heat capacity, and temperature of the fluid within Ω, respectively. The left-hand side of the equation quantifies the total change in internal energy within the control volume Ω. In contrast, the right-hand side represents the net energy flux crossing the boundary $\partial\Omega$, described by the scalar product between the generic thermal flux vector Φ_i and the local normal unit vector $\mathbf{n}$ to the boundary $\partial\Omega$. The flux is deemed positive if outgoing, and the tangential components of flow at $\partial\Omega$ do not contribute in terms of energy change within the control volume. The primary thermal contributions are summarized by [43]:

$$\Phi_{diffusive} = -\lambda\nabla T \tag{2}$$

$$\Phi_{advective} = \dot{\mathbf{m}}\, c_p\, T \tag{3}$$

$$\Phi_{radiative} = \mathbf{q}_{sun} \tag{4}$$

$$\Phi_{evaporative} = \dot{\mathbf{m}}_{evap}\, h_{gl}(T). \tag{5}$$

In the expressions above, λ represents the thermal conductivity, and h_{gl} denotes the latent heat of vaporization. Additionally, $\dot{\mathbf{m}}$ and $\dot{\mathbf{m}}_{evap}$ indicate the specific liquid mass flow rate passing through the control volume and the specific evaporative mass flow rate, respectively, both measured in units of [kg m^{-2} s^{-1}]. Furthermore, $\mathbf{q}_{sun}$ represents the incoming specific solar thermal energy absorbed on the feed side. Substituting the introduced thermal contributions into Eq. 1, we get:

$$\begin{aligned}\frac{d}{dt}\int_{\Omega}\rho c_p T\, d\Omega = &-\oint_{\partial\Omega}(\Phi_{diffusive}+\Phi_{advective})\cdot\mathbf{n}\, d\Sigma+\\ &-\oint_{\partial\Omega}(\Phi_{radiative}+\Phi_{evaporative})\cdot\mathbf{n}\, d\Sigma.\end{aligned} \tag{6}$$

Since the boundary $\partial\Omega$ has been assumed to be fixed over time, the previous equation can be rewritten as:

$$\begin{aligned}\int_{\Omega}\frac{\partial}{\partial t}(\rho c_p T)\, d\Omega = &-\oint_{\partial\Omega}-\lambda\nabla T\cdot\mathbf{n}\, d\Sigma+\\ &-\oint_{\partial\Omega}\dot{\mathbf{m}}\, c_p\, T\cdot\mathbf{n}\, d\Sigma-\oint_{\partial\Omega}\mathbf{q}_{sun}\cdot\mathbf{n}\, d\Sigma+\\ &-\oint_{\partial\Omega}\dot{\mathbf{m}}_{evap}\, h_{gl}(T)\cdot\mathbf{n}\, d\Sigma.\end{aligned} \tag{7}$$

The module of the evaporating mass flow rate $\dot{m}_{evap}$ at the membrane dividing the feed and permeate channels is influenced by the temperatures and salt concentration at the boundary, which affect the vapor pressure difference Δp_v across the membrane. The relationship is expressed as [43]:

$$\dot{m}_{evap} = K_v\,\Delta p_v, \tag{8}$$

where K_v represents the permeability coefficient of the membrane (measured in [kg Pa^{-1} m^{-2} s^{-1}]), which accounts for molecular and Knudsen diffusion and that can be defined as [44].

$$K_v = \frac{m_w}{RT}\left(\frac{p_a\tau\delta_m}{\epsilon_m p D_{wa}}+\frac{3\tau\delta_m}{\epsilon_m d_p}\sqrt{\frac{\pi m_w}{8RT}}\right)^{-1}. \tag{9}$$

Here, m_w represents the molar mass of water, R the universal gas constant, and T the average temperature across the membrane. The parameters p_a, p, δ_m, ϵ_m, τ, d_p, and D_{wa} denote, respectively, the partial and total pressure of air in the membrane pores, membrane thickness, membrane porosity, tortuosity, average diameter of the pores, and molecular diffusion coefficient of water vapor in air, respectively. The partial pressure of air (p_a) is calculated as the difference between the total atmospheric pressure and the water vapor pressure.

Furthermore, the vapor pressure difference across the membrane, Δp_v, is given by [44]:

$$\Delta p_v = a\left(Y_{feed}\right)p_v\left(T_{feed}\right)-a\left(Y_{permeate}\right)p_v\left(T_{permeate}\right). \tag{10}$$

In this equation, $a\left(Y_{feed}\right)$ and $a\left(Y_{permeate}\right)$ are the water activities of feed and permeate solutions, respectively, influenced by the mass fractions of salt (Y_{feed} and $Y_{permeate}$) under the hypothesis of diluted solutions. In detail, the activity of an NaCl aqueous solution can be estimated as $a = \frac{m_{\mathrm{NaCl}}(1-Y)}{m_{\mathrm{NaCl}}(1-Y)+N_{ion}m_w Y}$, where $N_{ion} = 2$ for NaCl, and m_{NaCl} and m_w are the molar masses in grams per mole of sodium chloride and water, respectively [44]. For the inlet feed water, a salinity of 35 g/L ($Y_{feed} = 0.035$) was considered, which is typical for seawater. The equation predicts $a\left(Y_{feed}\right)\approx 0.98$, while for distilled water, the activity is $a\left(Y_{permeate}\right) = 1$. It

is important to note that the developed 2D model evaluates $a(Y_{feed})$ locally within the feed channel, accounting for local concentration variations. The temperatures at the interface of the membrane in the feed and permeate channels are denoted by T_{feed} and $T_{permeate}$, respectively. Vapor pressures ($p_v(T)$) for pure water are determined using Antoine's semi-empirical correlation [44]:

$$p_v(T) = exp\left(23.1964 - \frac{3816.44}{T - 46.13}\right), \tag{11}$$

where p_v is measured in Pascals (Pa) and T in Kelvin (K).

Regarding mass transfer in the feed channel and thus the study of salt concentration, the continuity equation can be applied to the same fixed Eulerian control volume Ω, namely [45]:

$$\frac{d}{dt}\int_{\Omega} \rho c \, d\Omega = -\oint_{\partial\Omega} \left(\Phi^{*}_{diffusive} + \Phi^{*}_{advective}\right)\cdot \mathbf{n} \, d\Sigma \tag{12}$$

where the term on the left-hand side indicates the total change in solute mass within the control volume Ω, while the term on the right-hand side accounts for the mass flow through the boundaries, represented by the scalar product between the generic mass flow vector Φ and the local normal unit vector $\mathbf{n}$ to the boundary $\partial\Omega$. This unit vector is considered positive if it is outward facing. In the provided formulation, the variable c is the solute concentration. The right-hand side of the equation includes both diffusive and advective transport terms. The diffusive term is formulated as $\Phi^{*}_{diffusive} = -D_{Fick}\rho\nabla c$, where D_{Fick} represents the diffusion coefficient of the solute in water. The advective term is represented as $\Phi^{*}_{advective} = \dot{\mathbf{m}}c$, where $\dot{\mathbf{m}}$ is the specific liquid mass flow rate, measured in [kg m^{-2} s^{-2}]. Given these definitions and assuming that the boundary $\partial\Omega$ remains fixed over time, the continuity equation can be reformulated as follows [45]:

$$\int_{\Omega}\frac{\partial}{\partial t}(\rho c)\, d\Omega = -\oint_{\partial\Omega} - D_{Fick}\rho\nabla c\cdot\mathbf{n}\, d\Sigma + \\ -\oint_{\partial\Omega}\dot{\mathbf{m}}\, c\cdot\mathbf{n}\, d\Sigma. \tag{13}$$

2.2. Numerical model

The previous equations form the basis of a numerical model used to evaluate the performance of the solar enhanced DCMD module for seawater desalination. Our focus is primarily on the feed side of the module, utilizing the geometric symmetry on the z axis (see Fig. 1) to streamline the modeling process. The feed channel is discretized using 2D rectangular cells, each characterized by a central temperature that represents the fluid's thermal state, crucial for calculating diffusive heat flows. Additionally, temperatures at the four faces of each cell (top, bottom, left, right) are computed for evaluating advective heat flows. The temperatures of the top and bottom faces of each cell are calculated using the arithmetic mean of the central temperatures of the vertically adjacent cells. The temperature of the right face integrates six temperatures: the central temperatures of horizontally adjacent cells, alongside their top and bottom temperatures, including diagonally adjacent points. This approach accurately depicts thermal gradients and heat transfer, especially in scenarios involving advective flow.

Geometrical symmetry is also applied in modeling the membrane, with segmentation into the feed and permeate sides, each discretized into cells defined solely by their central temperature. Lateral face temperatures are disregarded due to the no-slip condition along x axis, which eliminates advective flows in these directions. The vertical advective flow entering the faces of the membrane cells is analyzed based on the temperature of the fluid-containing cell directly in contact. This discretization approach is also applied to study the salt transport. This structured meshing approach ensures consistent cell density per unit length across varying module dimensions, promoting error uniformity and enabling comparably consistent and mesh-independent results between different experimental setups. Such consistency is essential for accurately analyzing thermal and mass flows. To determine the optimal mesh resolution, a convergence study was conducted and is presented in Supplementary Note 2. This analysis evaluates the impact of varying node densities along both the x- and z-axes on local productivity. The results confirm that refining the mesh beyond the adopted resolution – 180 nodes/m along the x-axis and 18 nodes/mm along the z-axis – does not yield significant accuracy improvements, validating the selected discretization.

For the boundary conditions of the solar-enhanced DCMD model, the upper edge of the feed channel receives a heat flux representing the solar input (q_{sun}), while the lower edge in contact with the membrane experiences an outgoing specific heat flux due to latent heat from water evaporation and conductive losses through the membrane, that is:

$$\phi_{z=0} = q_{sun}\, A \tag{14}$$

$$\Phi_{z=\delta} = \dot{m}_{evap}h_{gl}(T) + \frac{\lambda_m}{\delta_m}\left(T_f - T_m\right). \tag{15}$$

Here, A denotes the direct solar-absorbing surface, assumed to be equal to the membrane surface, λ_m represents the thermal conductivity of the membrane, δ_m is the thickness of the membrane through which conduction occurs, T_f is the temperature of the feed channel at the membrane surface, and T_m is the temperature inside the membrane.

Then, for the sake of continuity, the specific heat flux at the permeate-membrane interface can be written as:

$$\Phi_{z=\delta+\delta_m} = \dot{m}_{evap}h_{gl}(T) + \frac{\lambda_m}{\delta_m}\left(T_m - T_p\right), \tag{16}$$

where T_p is the temperature of the permeate channel at the membrane surface. The convective losses from the back side of the module to the environment can be evaluated as:

$$\phi_{z=2\delta+\delta_m} = h\, A\left(T_p - T_{ext}\right), \tag{17}$$

where the term h is the convective heat transfer coefficient, which characterizes the heat transfer between the permeate channel and the external environment. A is the surface area through which convection occurs, T_p is the temperature of the permeate channel at the external surface and T_{ext} is the temperature of the external environment. Both lateral surfaces of channels are considered as well insulated, namely $\forall\, z$ and for $x = 0$ and $x = L$, the following condition holds:

$$\frac{\partial T}{\partial x} = 0\Big|_{\forall z\wedge(x=0\vee x=L)}. \tag{18}$$

The boundary conditions for the salt concentration are defined to prevent any salt exchange, especially near the membrane, where advective salt transport is canceled by evaporation. This accurately represents the increase in saline concentration due to water evaporation in the feed channel:

$$\dot{m}_s\Big|_{\forall x\wedge z=\delta} = 0 \tag{19}$$

$$\frac{\partial c}{\partial x}\Big|_{\forall z\wedge(x=0\vee x=L)} = 0 \tag{20}$$

$$\frac{\partial c}{\partial z}\Big|_{\forall x\wedge(z=0\vee z=\delta)} = 0, \tag{21}$$

being $\dot{m}_s$ the mass flow rate of salt.

A DCMD module typically consists of multiple square or rectangular channels arranged in parallel. In our model, we assume that the velocity profile within these channels resembles that of a cylindrical conduit according to Poiseuille's law. Analyzing the vertical section of a channel,

the inlet velocity distribution follows a parabolic trend. In particular, the no-slip condition ensures that velocity is zero at $z = 0$ and $z = \delta$, while at $z = 0.5\delta$ the velocity reaches its maximum value, which is twice the mean velocity. The inlet velocity profile is fixed in time and it is given by [46]:

$$v = 8\, v_{inlet}\, \frac{z}{\delta}\left(1 - \frac{z}{\delta}\right). \tag{22}$$

The velocity profile in the rest of the channel is obtained by applying the mass conservation principle, considering the evaporative flow rate, which is uniformly distributed across all cells with the same x coordinate. Similarly, temperature and concentration at the inlet are defined as:

$$T = T_{inlet} \tag{23}$$

$$c = c_{inlet}. \tag{24}$$

These conditions remain constant over time at the inlets of both channels. The schematic diagram of the simulation model, including boundary conditions, is provided in Supplementary Note 3.

Regarding the initial conditions for the numerical iteration, we assume that, throughout both channels, temperature and concentration are initially uniform and equal to the inlet values:

$$T(t = 0) = T_{inlet} \tag{25}$$

$$c(t = 0) = c_{inlet}. \tag{26}$$

The time discretization employs an explicit method, with the time resolution ensuring model convergence. The primary focus remains on achieving steady state, with less emphasis placed on transient phase accuracy.

2.3. Experimental methods

The experimental setup utilized to validate the numerical model is a DCMD system in a counter-current flow arrangement. A Sterlitech cell with an active membrane area of 140 cm^2 was employed, with a module measuring 14.7 cm in length and 9.7 cm in width. The setup includes two narrow channels, each with a height of 0.19 cm, designed for the separate circulation of feed and permeate solutions. A hydrophobic commercial PVDF membrane (GVS, Italy) was used, characterized by a pore size of 0.2 μm and a thickness of 150 μm. This membrane has a high contact angle of 151° and a porosity of 83%, optimizing its effectiveness for membrane distillation. The thermal conductivity of PVDF is equal to 0.19 W/(m·K). Fig. 2 shows a schematic representation of the experimental setup.

During testing, saline water with an initial concentration of 35 g/L was circulated in the feed channel, with inlet temperatures varied across multiple runs to examine the thermal effects on distillation productivity. Simultaneously, freshwater with nominally zero solute concentration flowed continuously along the permeate channel at a constant temperature of 18 °C, reflecting ambient environmental conditions. The flow rates were maintained uniformly at 25 L/h in both channels. Temperature monitoring was conducted using type K thermocouples placed at the inlet and outlet of both channels to ensure precise thermal data collection. Data acquisition intervals were set at 3 min, focusing on flow dynamics and temperature variations to establish a comprehensive dataset reflective of steady-state conditions. The experimental trials were performed in triplicates, targeting feed inlet temperatures of 30 °C, 35 °C, and 40 °C, suitable for low-grade heat exploitation. However, due to limitations in temperature control, the actual mean temperatures achieved during the experiments were 30.81 °C, 35.61 °C, and 40.45 °C, respectively. This discrepancy does not affect the model validation, as the same actual inlet boundary conditions were used in the simulations.

Given the experimental setup, an estimated uncertainty margin of 15% was applied to flow rates and membrane characteristics. Model results were validated against experimental data by averaging scenarios in which these uncertainties either enhanced or reduced model efficiency, ensuring a comprehensive and balanced evaluation of experimental data relative to theoretical predictions.

3. Results

3.1. Model validation

Fig. 3 illustrates the productivity of a DCMD module in a range of feedwater inlet temperatures, while maintaining constant conditions for other operational parameters. The experimental results and their uncertainties (error bars) are plotted alongside model predictions, to validate the accuracy and reliability of the model.

The model predictions were generated by incorporating a 15% uncertainty in the critical characteristic parameters, namely, the feed flow rate, permeate flow rate, membrane thickness, pore size, membrane porosity, and membrane thermal conductivity. For the feed inlet temperature and permeate inlet temperature, an uncertainty of 2 °C was assumed. This approach allowed accounting for variations in productivity due to these uncertainties. The values shown in the graph represent the average of the minimum and maximum productivity values obtained from these parameter variations.

The experimental data points – 1.59, 2.87, and 4.33 L m^{-2} h^{-1} (LMH) – come with associated uncertainties of 0.09, 0.10, and 0.46 LMH,

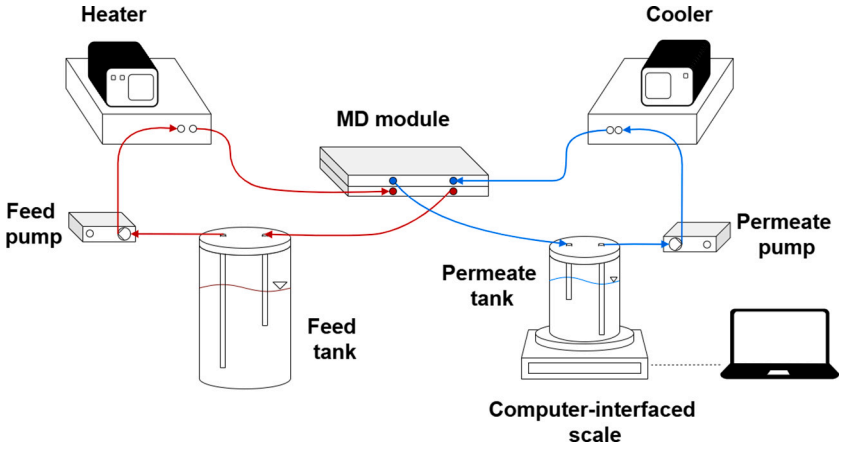

Fig. 2. Schematic representation of the experimental setup utilized to validate the model. In red, the feed circuit; in blue, the distillate circuit. The two solutions meet in the two plate module containing the membrane, and are then returned to the respective tank. Flux data were collected monitoring the change in weight of the permeate tank by means of a computer-interfaced scale.

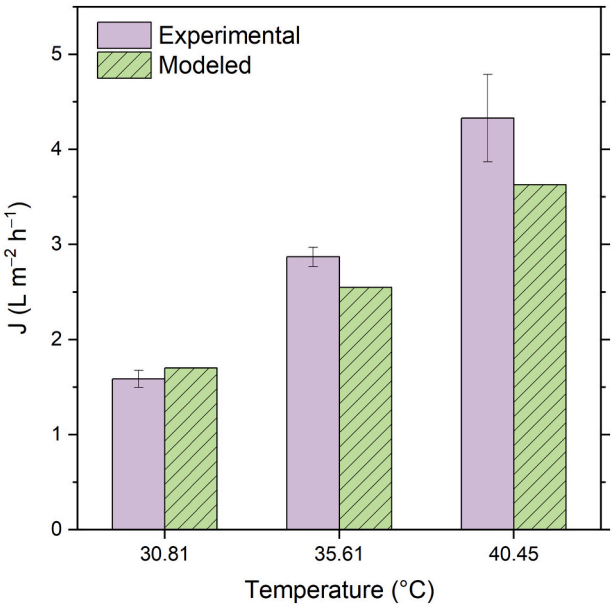

Fig. 3. Water flux of a direct contact membrane distillation (DCMD) module as a function of the feedwater inlet temperature. The graph compares experimental values with model predictions. The model values are calculated by considering a 15% uncertainty in the characteristic parameters, including feed flow rate, permeate flow rate, membrane thickness, pore size, membrane porosity, and membrane thermal conductivity. For the feed inlet temperature and permeate inlet temperature, an uncertainty of 2 °C was assumed.

respectively. In comparison, the model predictions are 1.70, 2.55, and 3.63 LMH. The observed discrepancies between the average experimental values and the model predictions ranged from +7% to −16%, therefore demonstrating a good prediction capability of the model. To further assess the model's accuracy, we computed the Mean Absolute Percentage Error (MAPE), Mean Absolute Error (MAE), and the Coefficient of Determination (R^2). The results are as follows: MAPE = 11.41%, MAE = 0.377 LMH, and R^2 = 0.839. These values indicate that the model provides a reasonably accurate representation of the experimental data. The MAPE suggests a moderate level of error, the MAE confirms a relatively small absolute deviation, and the R^2 value demonstrates a strong correlation between predicted and experimental values. This statistical assessment reinforces the validity of the model in capturing the key trends of the system. Moreover, the model successfully captures the trend of increasing productivity with rising feedwater inlet temperatures, although the model slightly underpredicts the absolute productivity values.

Overall, the validation exercise confirmed that the model can reliably represent trends of the DCMD system productivity. The model can thus be exploited to analyze and optimize the performance of the DCMD modules, extending the exploration also to the effect of direct solar absorption on distillate productivity.

3.2. Model exploration

3.2.1. Detailed case studies

Before systematically exploring the effects of operating conditions and module configurations, we analyze selected case studies to gain a detailed understanding of the heat and mass transfer mechanisms in the DCMD module enhanced by direct solar absorption.

First, let us consider v_{inlet} equal to 1 mm/s, a module length of 25 cm, and a channel thickness of 0.5 mm; the module is for example subjected to a concentrated solar radiation intensity of 2000 W m^{-2}, the inlet temperature of the feed solution is set to 50 °C, and the system operates in a co-current configuration. Fig. 4a presents the steady state temperature distribution along the feed and permeate channels as predicted by the validated model. The maximum temperature in Fig. 4a reaches 90 °C on the feed side, consistently higher than the inlet temperature due to direct solar heating on the module surface. This high temperature enhances the vaporization rate, thereby increasing productivity. However, such elevated temperatures may also pose challenges, including larger scaling rates. Additionally, operating at high temperatures requires careful material selection and module design to ensure long-term durability and performance stability. The accompanying Fig. 4b shows the distribution of salt concentration in the feed channel, where a maximum of 48 g/L is reached at the outlet of the module, implying high local evaporation rates. As the fluid travels along the module, it becomes progressively more concentrated due to continuous evaporation of feedwater, leading to these elevated concentrations.

The module performance metrics predicted by the validated model for this first case study are as follows: productivity of 2.5 LMH, thermodynamic heat transfer efficiency of the membrane equal to 0.78 (calculated as the ratio of latent heat transferred by vapor to total heat transferred through the membrane), average temperature polarization coefficient (TPC, defined as the ratio between the mean temperature difference at the membrane surfaces and the difference between the inlet temperatures of the feed and permeate channels) of 0.04, and average salt concentration polarization coefficient (CPC, defined as the ratio between the mean concentration difference at the membrane surfaces and the difference between the inlet concentrations of the feed and permeate channels) of 1.20. These values indicate a relatively high heat transfer efficiency, suggesting that the majority of the heat transferred through the membrane contributes to vaporization, which is beneficial for energy efficiency. However, the average CPC of 1.20 indicates moderate salt accumulation near the membrane surface, which could also potentially impact long-term performance and require periodic maintenance.

In a second case study, the module is subjected to a solar radiation intensity of 2000 W m^{-2}, as in the first case. However, this configuration differs significantly in other parameters: the module length is 1 m, the channel thickness is 1 mm, the feed inlet temperature is 70 °C, and the inlet flow velocity is 10 mm/s. The system operates in a counter-current configuration. The model results in Fig. 4c illustrate the temperature distribution across the module. Unlike the first case, the maximum temperature does not exceed 80 °C. Coherently with the higher mass flow rate imposed, the temperature gradient is more evenly distributed and homogeneous, also reflecting the effectiveness of the counter-current configuration in maintaining a stable temperature profile along the module. This uniform temperature distribution enhances the overall thermal efficiency and reduce the risk of hot spots that could lead to scaling or membrane damage. Consequently, the distribution of salt concentration in the feed channel in Fig. 4d shows high salinity levels near the module outlet due to substantial feedwater evaporation. The concentration gradient is more pronounced than in the first case study, indicating elevated local evaporation rates at the exit thanks to the more homogeneous distribution of the temperature difference across the membrane.

Performance metrics calculated for this second case include a productivity of 4.7 LMH, an average TPC of 0.06, an average CPC of 1.27, and a heat transfer efficiency of 0.734. Compared to the first case study, this configuration exhibits a higher productivity, which is partly attributed to the higher inlet flow velocity and feed temperature. The TPC value indicates a slightly higher temperature, which suggests a greater degree of thermal resistance at the membrane surface due to a thicker channel and a more homogeneous temperature distribution. The higher TPC combined with the elevated feed temperature suggests a greater distributed productivity, which may explain the observed increase in CPC compared to the first case study.

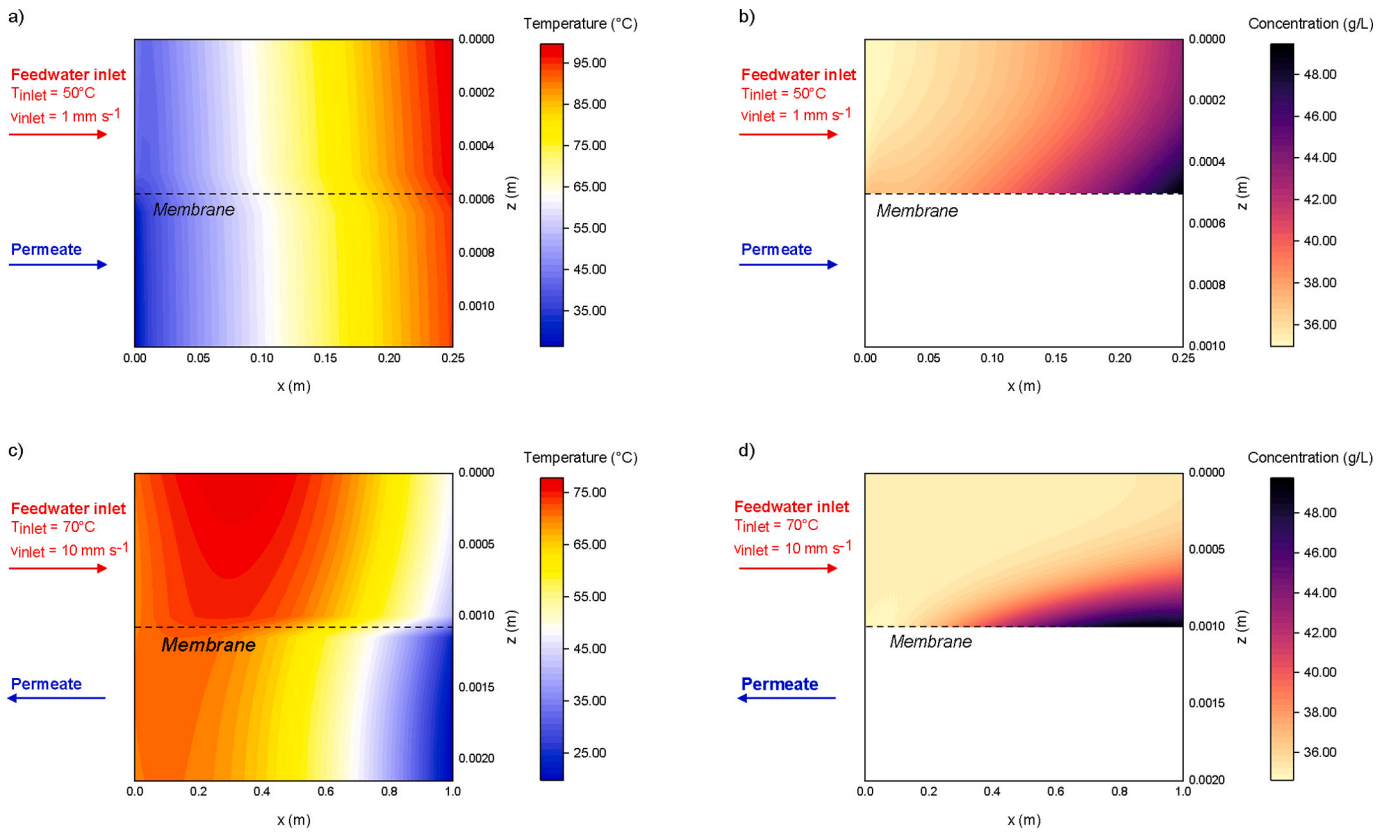

Fig. 4. Model results for DCMD module enhanced by direct solar absorption with two different flow velocities: (a) Temperature and (b) salt concentration distribution for v_{inlet} = 1 mm/s in co-current configuration; (c) temperature and (d) salt concentration distribution for v_{inlet} = 10 mm/s in counter-current configuration. Note that the membrane is positioned at mid z axis. The concentration distribution is not plotted on the permeate side, which is considered as distilled water. For the slow flow velocity (a and b), L and δ are equal to 25 cm and 0.5 mm, respectively. In the co-current configuration, the module operates under a solar radiation flux equal to 2000 W m^{-2}, with a fixed feed inlet temperature of 50 °C. For the medium flow velocity (c and d), L and δ are equal to 1 m and 1 mm, respectively. In the counter-current configuration, the module operates under a solar radiation flux equal to 2000 W m^{-2}, with a fixed feed inlet temperature of 70 °C. The permeate inlet temperature is considered at ambient conditions, that is 20 °C in all the considered case studies.

3.2.2. *Sensitivity analysis of solar enhancement*

Given the enhancements highlighted in Fig. 4, a dedicated sensitivity analysis of the direct solar absorption on the DCMD module performance was carried out. In this analysis, model results are reported in terms of the specific productivity J (Fig. 5), TPC (Fig. 6), and CPC (Fig. 7) as a function of the distance from the feed channel inlet, where saline water

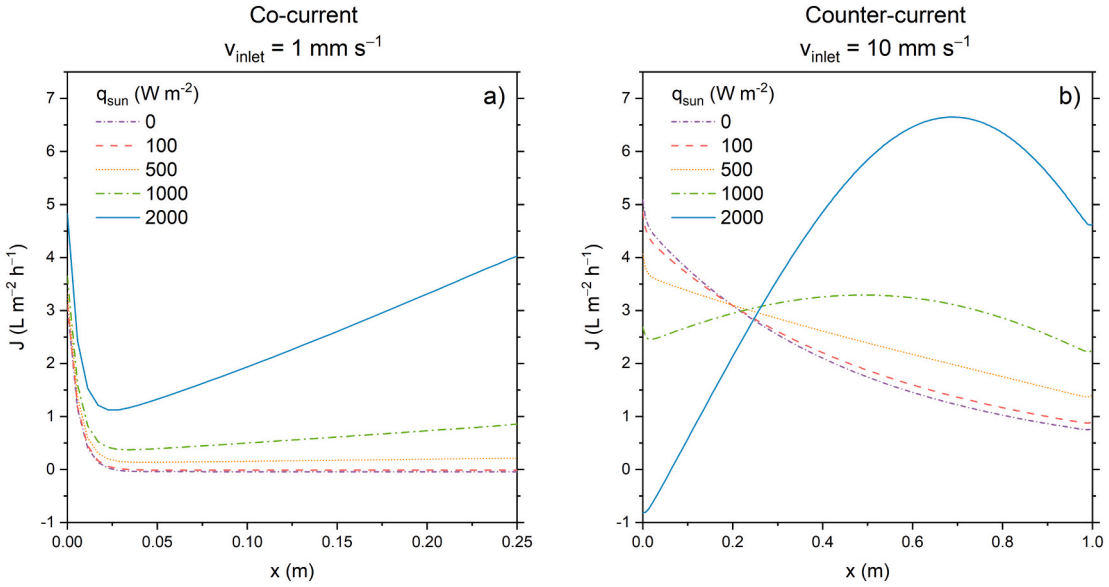

Fig. 5. Productivity of the solar-enhanced DCMD module as a function of coordinate x for two flow velocities and configurations, and for varying solar radiation levels: (a) 1 mm/s co-current, (b) 10 mm/s counter-current. The operating conditions and module geometry are the same as those described in Fig. 4.

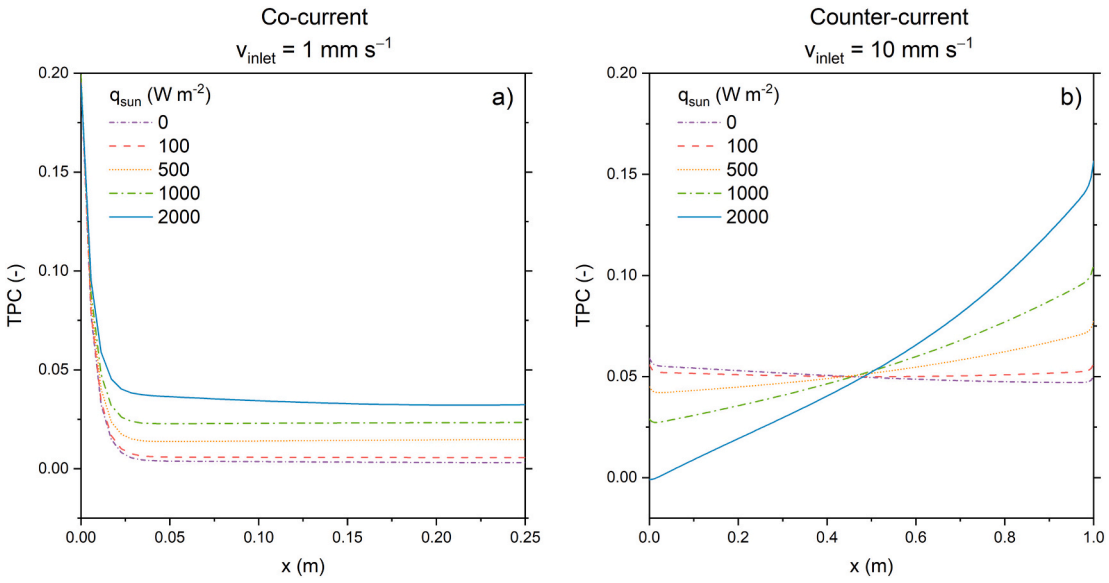

Fig. 6. TPC of the solar-enhanced DCMD module as a function of coordinate x for two flow velocities and configurations, and for varying solar radiation levels: (a) 1 mm/s co-current, (b) 10 mm/s counter-current. The operating conditions and module geometry are the same as those described in Fig. 4.

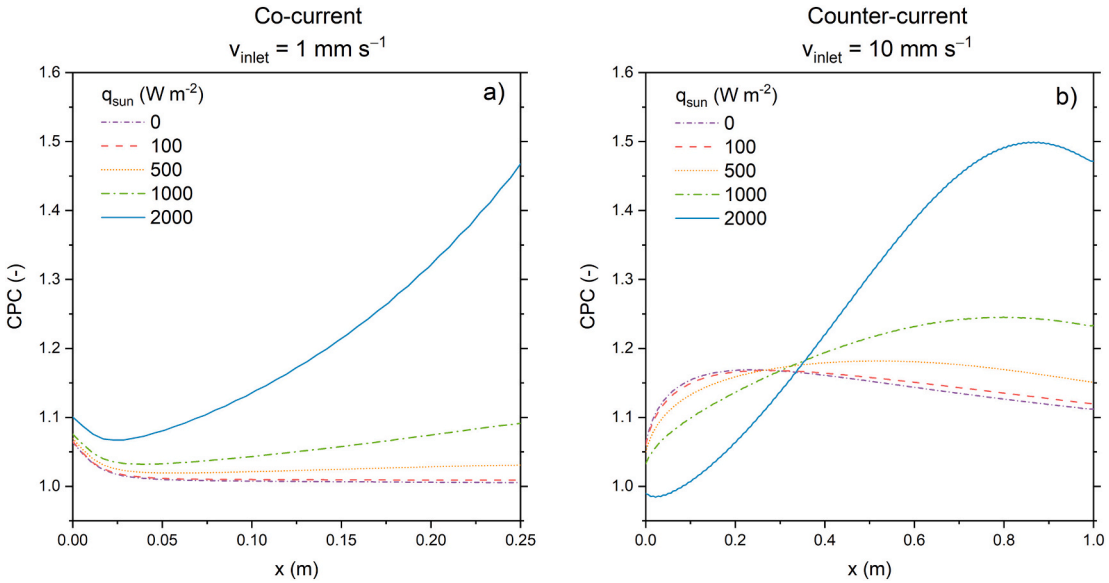

Fig. 7. CPC of the solar enhanced DCMD module as a function of coordinate x for two flow velocities and configurations, and for varying solar radiation levels: (a) 1 mm/s co-current, (b) 10 mm/s counter-current. The operating conditions and module geometry are the same as those described in Fig. 4.

flows. Multiple curves are presented, each corresponding to a different value of solar radiation: 0, 100, 500, 1000, and 2000 W m^{-2}. Notice that the considered solar irradiance values include both non-concentrated and concentrated sources. The latter can be achieved on flat plate solar collectors by means of adjustable flat mirrors [47] or solar tracking Fresnel lens [48], achieving moderate solar concentrations. The two case studies analyzed in Section 3.2.1 are considered again, namely: (a) co-current configuration with $v_{\text{inlet}} = 1$ mm/s, $L = 25$ cm, $\delta = 0.5$ mm, and feed inlet temperature of 50 °C; and (b) counter-current configuration with $v_{\text{inlet}} = 10$ mm/s, $L = 1$ m, $\delta = 1$ mm, and feed inlet temperature of 70 °C. The permeate inlet temperature is considered again at ambient conditions, that is 20 °C in all the considered case studies.

The results of the first case study, presented in Fig. 5a, show that, as solar radiation increases, the productivity of the module increases considerably, particularly in regions farther from the inlet. Considering the DCMD module without any solar enhancement, the peak productivity is observed near the inlet due to the co-current configuration. This conventional configuration creates the highest temperature gradient at the beginning of the feed channel, resulting in the maximum evaporative flux at the inlet. As feedwater progresses along the module, the temperature difference between feed and permeate decreases, causing a decline in the evaporation rate. Direct solar absorption, on the other hand, shows a marked increase in evaporative flux, especially toward the end of the feed channel. This increase indicates that higher solar radiation provides additional heat for evaporation, leading to greater productivity along the entire length of the module. The sharp rise of the 2000 W m^{-2} curve at the outlet highlights the substantial effect of high solar radiation on enhancing evaporation in the latter sections of the module.

Fig. 6a reveals that at the module inlet, the TPC values are highest, then rapidly decrease along the length of the feed channel. This trend is expected because the initial temperature difference between the feed

and permeate sides is greatest near the inlet, leading to lower temperature polarization. The rapid decrease in TPC values along the module length, which is mainly confined to the portion of the module close to the inlet, suggests that the flow configuration (co-current in this case study) faces challenges in maintaining high TPC as the feedwater progresses. This reduction in TPC along the channel leads to a loss in thermal gradient efficiency, which reduces the overall evaporative flux and productivity. As solar radiation increases, there is a noticeable impact on the TPC values. The 2000 W m^{-2} curve shows a higher initial TPC compared to the other curves, indicating lower temperature polarization due to the higher heat input. As the distance from the inlet increases, the TPC for all curves stabilizes and decreases to lower values, despite configurations with higher direct solar absorption maintaining higher TPC values (that is, lower temperature polarization).

The CPC values in Fig. 7a indicate the extent of salt concentration polarization within the module. Higher CPC values suggest a higher degree of salt accumulation near the membrane surface, which reduces distillation performance. Ideally, lower CPC values (i.e. ideally equal to 1) are preferable to minimize polarization effects. CPC values are initially high at the module's inlet, especially for higher levels of solar radiation. As the distance from the inlet increases, the CPC values for all radiation levels initially decrease, indicating a reduction in salt concentration polarization. However, beyond a certain point, the CPC values start to rise again, particularly for higher radiation levels. The 2000 W m^{-2} curve shows the highest initial CPC, which then decreases sharply and rises again toward the end of the feed channel. This pattern suggests substantial salt accumulation even near the inlet due to high evaporation rates caused by increased solar radiation. From Fig. 6a, it can be observed that although the temperature difference remains constant along the module axis, productivity increases because the absolute temperature rises. In fact, vapor pressure and temperature are linked by a exponential relationship.

The second case study in Fig. 5b shows that, due to the counter-current configuration, the increased solar radiation produces different effects compared to the first case. Higher solar radiation leads to a warmer permeate near the feed inlet, which results in locally reduced productivity. This effect is seen in the initial section of the feed channel, where the temperature difference between the feed and permeate is lower, reducing the driving force for evaporation. However, overall productivity increases with higher solar radiation levels. This result occurs because the temperature gradient at the feed outlet is considerably enhanced, promoting a higher evaporative flux toward the end of the channel. The counter-current configuration effectively utilizes the increased thermal energy, maintaining a substantial temperature difference across the length of the module and thereby boosting the overall evaporation rate.

In this counter-current configuration, the TPC values in Fig. 6b start lower and gradually increase along the length of the feed channel. This trend contrasts with the first case, where TPC values were highest at the inlet and decreased along the channel. The 2000 W m^{-2} curve exhibits the lowest initial TPC, which then rises toward the end of the feed channel, indicating a lower polarization extent at the outlet due to higher solar radiation. The other curves follow a similar pattern, with the TPC values increasing more steeply at higher radiation levels. The counter-current configuration allows for better temperature distribution along the module, as the warmest permeate meets the coolest feed at the outlet, maintaining a higher temperature gradient and thus improving TPC values as the distance increases. This configuration more effectively utilizes the thermal energy from solar radiation, ensuring a more consistent and higher TPC along the module length.

In the second case, the CPC values start relatively low at the inlet and gradually increase along the length of the feed channel (see Fig. 7b). The 2000 W m^{-2} curve shows an important rise, peaking toward the end of the channel before slightly decreasing. This trend indicates that higher solar radiation levels lead to more substantial salt accumulation due to increased evaporation rates. Notably, the 2000 W m^{-2} curve initially displays a CPC value of less than one, suggesting a reverse flow phenomenon where vapor flows from the permeate side back to the feed side near the inlet. This reverse flow can occur due to the high temperature and pressure gradient induced by the intense solar radiation, which heats the permeate flow. Following this initial reverse flow, the CPC increases sharply. The other curves exhibit a more gradual trend, with CPC values rising steadily and not displaying the initial values below one seen in the blue (2000 W m^{-2}) curve.

3.2.3. Productivity maps

In Fig. 8, a systematic sensitivity analysis of the specific productivity (J, expressed in LMH) of the DCMD module with enhanced performance by direct solar absorption is depicted. Model results are reported as a function of various operational parameters and module configurations, including channel height (δ), module length (L), average input velocity (v_{inlet}), feed solution temperature (T_{feed}), and solar radiation directly absorbed on the feed side (q_{sun}). Specifically, the channel heights δ were set to 0.5, 1, 2, 3, and 5 mm; the module lengths L to 10, 25, 50, and 100 cm; the inlet average velocities of the feed solution to 1 mm/s (slow flow), 10 mm/s (medium flow), 100 mm/s (fast flow); and the inlet temperatures of the feed solution to 30 °C, 40 °C, 50 °C, 60 °C, and 70 °C. Moreover, five values of solar radiation were considered, namely 0q, 0.1q, 0.5q, 1q, and 2q, where q is equal to 1 kW m^{-2}. Note also that values above the horizontal axes represent the co-current (EC) configuration, while those below represent the counter-current (CC) configuration.

In all scenarios, the temperature of the permeate inlet was set to 20 °C, equal to the ambient temperature. Furthermore, a convective heat transfer coefficient h equal to 10 W/(m^2 K) (assuming natural convection) was considered to account for the thermal losses from the permeate channel to the environment, while other heat losses were neglected. The membrane used in the model has the following characteristics: porosity ε_m equal to 0.83, thermal conductivity of the porous material λ_m equal to 0.019 W/(m K), thickness δ_m equal to 150 μm, and pore radius d_p of 0.20 μm. Notably, combinations of parameters leading to local feed temperatures over 100 °C are excluded from the plots since boiling shall be avoided in MD modules.

First of all, it is worth noting that the counter-current configuration, represented by values below the horizontal axes, tends to show higher specific productivity compared to the co-current configuration due to the more homogeneous temperature gradient along the module.

Furthermore, a general positive effect of higher fluid velocity on J can be also noticed, due to improved heat and mass transfer mechanisms in the module channels. As expected, higher feed temperatures (50 °C, 60 °C, and 70 °C) increase productivity, with maximum values at 70 °C, due to an enhanced thermal gradient driving the distillation process. These results align with the expected behavior of traditional DCMD modules using only bulk heating ($q_{sun} = 0$ W m^{-2}), where productivity increases with both Reynolds number (enhancing heat and mass transfer) and feedwater temperature (providing more available thermal energy) [49]. Figure in Supplementary Note 4 reports a detailed analysis of model predictions for this scenario.

Increased solar radiation boosts specific productivity too, as additional solar energy heats the fluid, improving the temperature gradient and process efficiency.

The overall trend shows that specific productivity decreases with increasing module length. Shorter modules (10 cm and 25 cm) exhibit higher productivity than longer ones (50 cm and 100 cm), attributed to lower heat losses and a more sustained temperature gradient along the shorter module. However, interesting deviations from this trend, particularly under distributed solar radiation, are observed and will be analyzed and discussed later.

The influence of channel height on productivity is more subtly affected by specific parameter sets and flow velocities. For shorter module lengths (10 cm and 25 cm) and slow to medium velocities (1

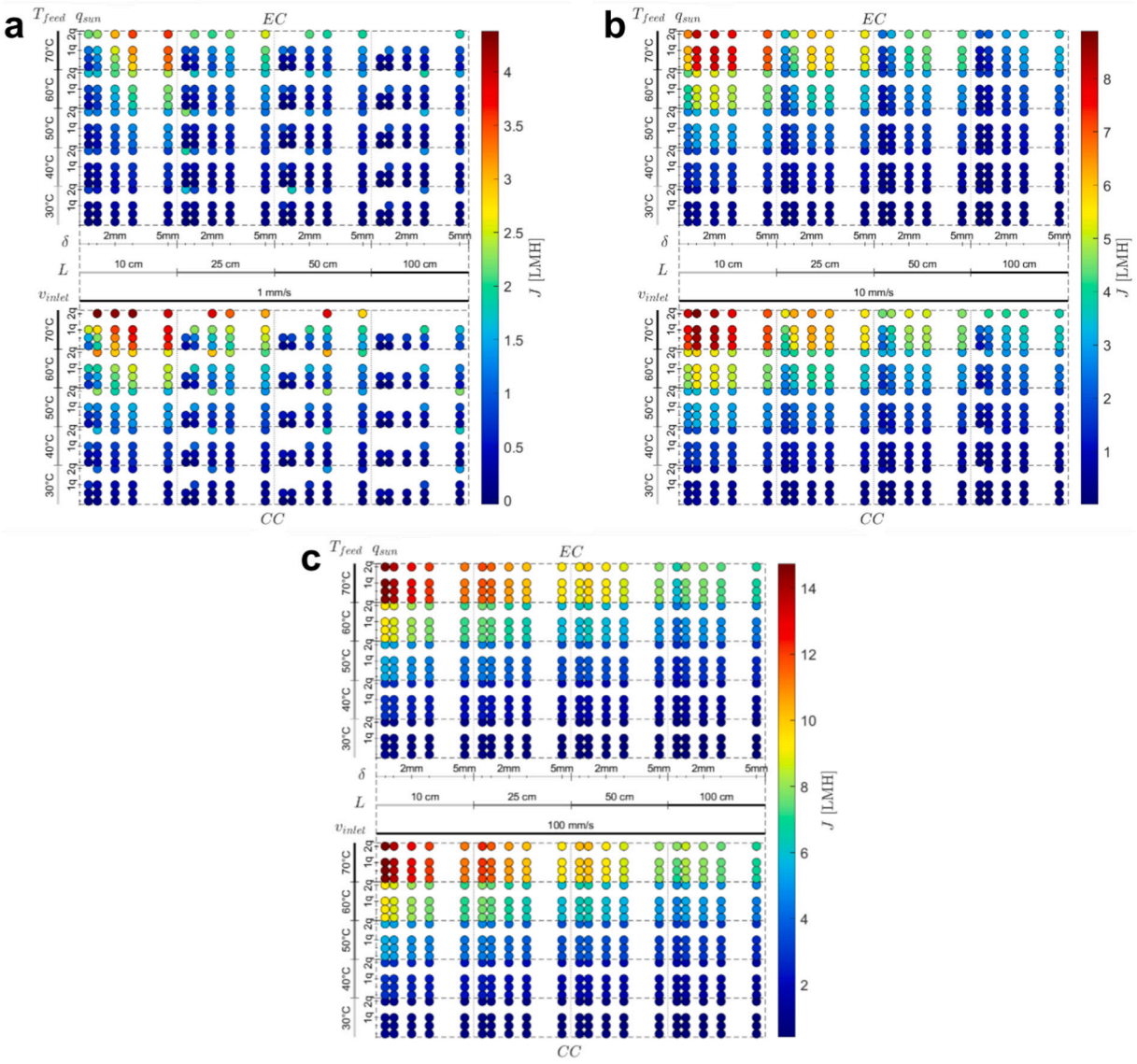

Fig. 8. Specific productivity J of the DCMD module enhanced with direct solar absorption under different flow velocities: (a) low flow velocity (namely, v_{inlet} equal to 1 mm/s), (b) medium flow velocity (namely, v_{inlet} equal to 10 mm/s), and (c) high flow velocity (namely, v_{inlet} equal to 100 mm/s). Data are categorized by channel height δ (0.5, 1, 2, 3, and 5 mm); module length L (10, 25, 50, and 100 cm); feed temperatures T_{feed} (30 °C, 40 °C, 50 °C, 60 °C, and 70 °C); and solar radiation q_{sun} ($0q$, $0.1q$, $0.5q$, $1q$ and $2q$, where q is equal to 1 kW m^{-2}). Values above the horizontal axis indicate the co-current configuration (EC), while those below represent the counter-current (CC) configuration.

mm/s and 10 mm/s) in the co-current (EC) configuration with feed temperatures above 50 °C, an increase in channel thickness leads to higher productivity. Instead, in counter-current (CC) configuration with high solar radiation, increasing the channel height decreases productivity regardless of the temperature. For longer lengths (50 cm and 100 cm) in both EC and CC configurations, increasing thickness negatively affects productivity in most of the configurations, likely due to the increased thermal resistance introduced by thicker channels, which limits the efficiency of the distillation process.

To better appreciate the possible beneficial effect of direct solar absorption on module performance, Fig. 9a illustrates the logarithmic variation of productivity, $log_{10}(1 + \Delta J/J_{ref})$, under different conditions of channel height, module length, feed temperature, and solar radiation for both co-current and counter-current flow configurations at a low inlet velocity of 1 mm/s. Here, J_{ref} represents the minimum productivity of each sector, determined by specific values of L and T_{feed}. This generally corresponds to the condition of no solar radiation ($q_{sun} = 0$) and a channel thickness of 0.5 mm (the lowest considered). However, under these conditions, productivity can occasionally become negative if reverse flow dominates. In the graph, points with negative productivity have been removed. This approach highlights the influence of solar radiation and channel height on ΔJ, i.e., the variation in productivity relative to the reference case.

The influence of solar radiation is evident in Fig. 9a, particularly at higher levels of $q_{sun} = 2q$, which significantly boosts productivity gain (ΔJ) at lower feed temperatures (30–50 °C) and longer module lengths (50 cm and 100 cm). This is highlighted by the orange to red regions in the color map, indicating gains above a factor of 2.5. At higher feed temperatures (60–70 °C), the effect of solar radiation diminishes, with most data points falling within the blue-green range, signaling minimal productivity gains, except when the module length reaches 1 m, where gains are more considerable. Increasing the channel height can lead to either higher or lower productivity, with the effect being more pronounced in the EC configuration. However, for shorter modules (10 cm, 25 cm), the impact of channel height on productivity is limited, as shown by the prevalence of blue and light green points. The highest

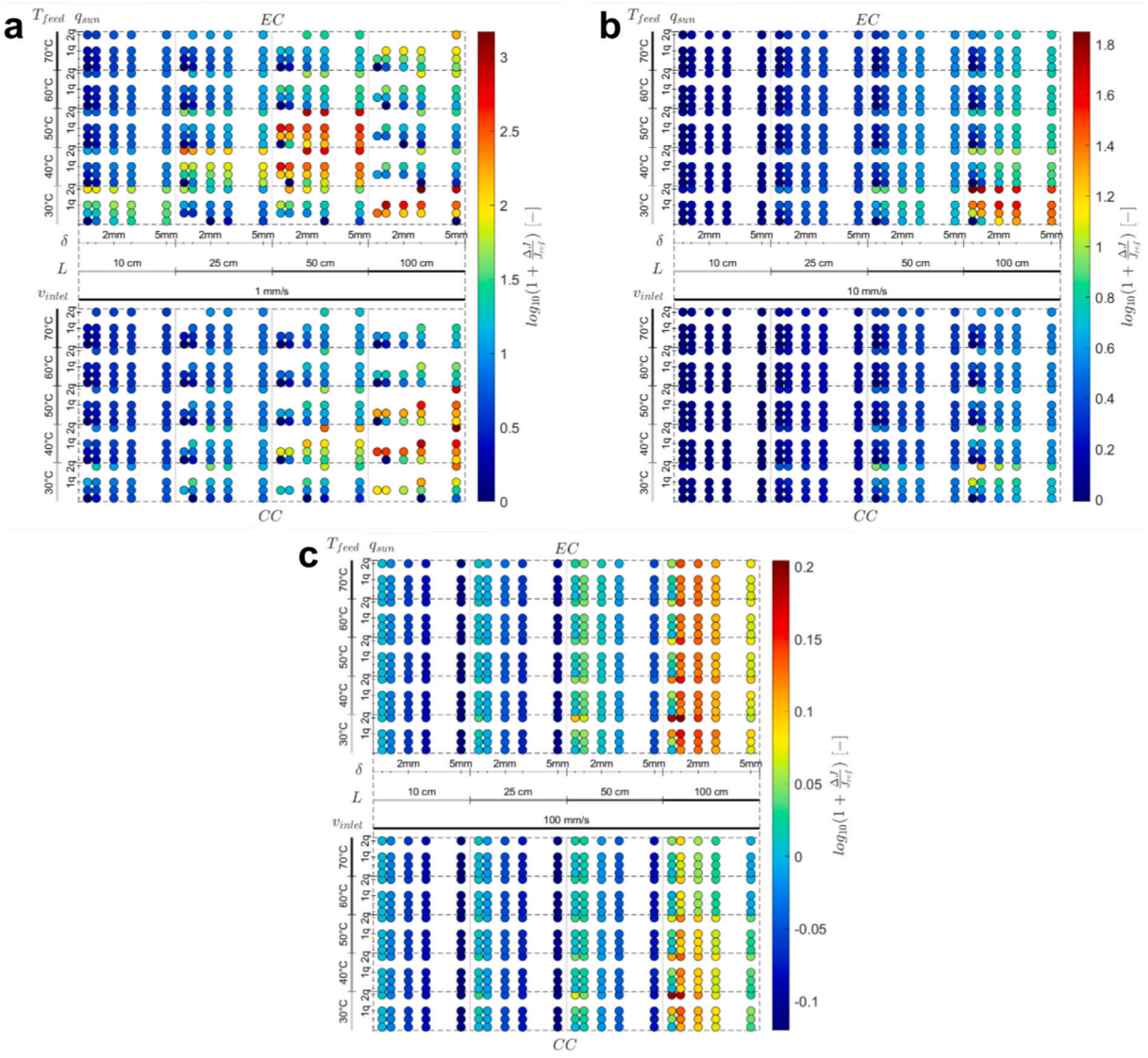

Fig. 9. Logarithmic variation of productivity, expressed as $log_{10}(1+\Delta J/J_{ref})$, for the DCMD module with direct solar absorption under different flow velocities: (a) low flow velocity (v_{inlet} = 1 mm/s), (b) medium flow velocity (v_{inlet} = 10 mm/s), and (c) high flow velocity (v_{inlet} = 100 mm/s). Here, J_{ref} represents the minimum productivity of the sector, which generally corresponds to the condition of no solar radiation (q_{sun} = 0) and a channel thickness of 0.5 mm (the lowest considered). However, under these conditions, productivity can occasionally become negative if reverse flow dominates. In the graph, points with negative productivity have been removed. This approach highlights the influence of solar radiation and channel height on ΔJ, i.e., the variation in productivity relative to the reference case. The variation in these two parameters, in particular, affects the volumetric absorption of solar radiation. Data are categorized by channel height δ (0.5, 1, 2, 3, and 5 mm); module length L (10, 25, 50, and 100 cm); feed temperatures T_{feed} (30 °C, 40 °C, 50 °C, 60 °C, and 70 °C); and solar radiation q_{sun} (0q, 0.1q, 0.5q, 1q and 2q, where q is equal to 1 kW m^{-2}). Values above the horizontal axis indicate the co-current configuration (EC), while those below represent the counter-current (CC) configuration.

productivity gains occur under a combination of high solar radiation (2q), lower feed inlet temperatures (30–50 °C), medium channel heights (2 mm), and longer modules (50–100 cm), where the bright red regions in the figure highlight optimal performance. The CC configuration consistently exhibits slightly lower productivity gains compared to EC under similar conditions, with reduced sensitivity to solar radiation. The data points showing the highest productivity gains are associated with the maximum module length of 1 m.

For the case of medium velocity (10 mm/s), Fig. 9b, the influence of solar radiation and channel height on productivity gain is less pronounced compared to the low-velocity case. The relative productivity enhancement is lower, as indicated by a reduced range of color intensity on the scale, with the maximum gain just above 1.8. However, some trends remain consistent, particularly the fact that higher solar radiation (2q) at higher feed inlet temperatures (50 °C–70 °C) and longer module lengths (50 cm, 100 cm) still provide the highest gains, albeit with lower absolute values compared to the low-velocity case. The EC configuration once again exhibits slightly higher gains than the CC configuration. The height of the channel continues to affect productivity, with larger heights (5 mm) resulting in higher gains, particularly at higher temperatures and longer modules. Nevertheless, the medium velocity condition shows a general reduction in the impact of both solar radiation and channel height, with much of the data remaining in the blue-to-green range, indicating smaller productivity variations.

For the case of high velocity (100 mm/s), Fig. 9c, the overall variation in productivity is considerably lower compared to both the low- and medium-velocity cases. The color map scale shows a maximum gain just above 0.2, indicating that the influence of both solar radiation and channel height is much less pronounced at this high velocity. However, the trends observed in previous cases still hold to some extent. Higher solar radiation (q_{sun} = 2q) continues to lead to the highest productivity gains, particularly at feed temperatures of 50 °C–70 °C and longer

module lengths (50 cm, 100 cm), with the highest channel height (5 mm) still showing the most favorable results. The EC configuration again exhibits higher gains compared to the CC one, though the difference is minimal at this fluid velocity, with most of the data points across both configurations falling within the blue-to-light green range. Productivity gains at high velocity are reduced, especially in shorter modules (10 cm, 25 cm) and at lower feed temperatures (30 °C–40 °C), where almost no productivity gains are observed, as shown by the dominance of dark blue points. Overall, under high velocity, the productivity enhancements from direct solar radiation and channel height are minimal, suggesting that high flow velocities reduce the sensitivity of the system to these parameters.

Additionally, a detailed analysis of specific energy consumption is provided in Supplementary Note 5. This study evaluates energy efficiency across different operating conditions, showing that specific energy consumption decreases for longer module lengths (0.5 m and 1 m), approaching the thermodynamic limit. These insights contribute to a broader understanding of system performance, complementing the productivity analysis and enabling a comparison with other solar thermal desalination technologies.

4. Discussion

The results indicate that the maximum productivity values are predicted in the counter-current configuration at medium-to-high feed flow velocities. As expected, productivity also increases when operating at high feed temperatures (60–70 °C) and solar radiation intensities (1000–2000 W m^{-2}). Specifically, a productivity enhancement as high as 2.5 times may be obtained (in case of the lowest fluid flows) under 2000 W m^{-2} compared to modules without solar input. While solar radiation increases productivity across the module, its effect is most significant in the later sections of the module, due to cumulative heating. However, note that high productivity conditions may intensify the salt concentration polarization effect (CPC values above 1.2), requiring effective strategies to manage the consequent high salinity values and mitigate potential scaling effects.

A more detailed analysis of the results unravels that similar, or even higher water fluxes may be achieved by reducing the feed inlet temperature while increasing the solar radiation intensity. Indeed, given the same configuration, different cases show that the predicted productivity at 30 °C with solar radiation of 2 kW m^{-2} exceeds the one estimated at

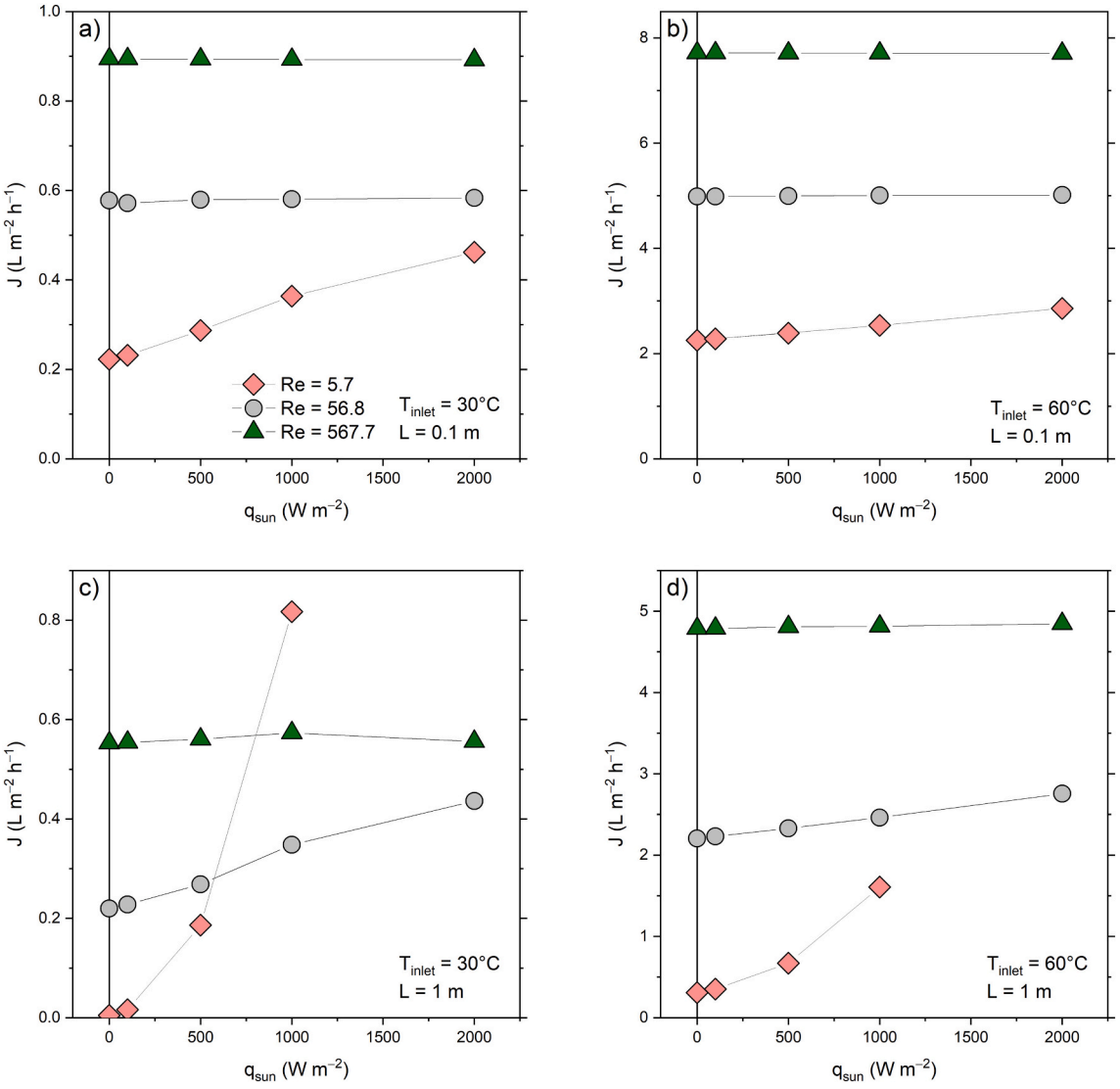

Fig. 10. Specific productivity J predicted by the model for a counter-current DCMD module with direct solar heating (q_{sun}). Results are shown with respect to different Reynolds numbers (Re), while fixing the feed channel thickness ($\delta = 3$ mm) and considering different values of feedwater temperature at the inlet and module length: (a) $T_{inlet} = 30$ °C and $L = 0.1$ m; (b) $T_{inlet} = 60$ °C and $L = 0.1$ m; (c) $T_{inlet} = 30$ °C and $L = 1.0$ m; (d) $T_{inlet} = 60$ °C and $L = 1.0$ m. The lines connecting the individual data-points are solely meant as a guide for the eye.

70 °C without solar radiation. This input power reduction theoretically decreases the overall thermal energy consumption of the system leading also to reduced capital costs related to heating systems and heat exchangers. As an example, reducing the inlet temperature from 70 °C to 30 °C could lead to an energy save of around 46.5 kWh m^{-3} (calculating the difference of provided heat as $\Delta Q = m\, c_p\, \Delta T$, where m is the mass of water to be heated and ΔT the temperature difference — in this case 40 °C).

The contribution of solar radiation on productivity becomes particularly advantageous when operating at low flow velocities, low inlet temperatures and longer modules, as depicted in Fig. 10, where specific productivity J is shown as a function of solar radiation for different Reynolds numbers (hence flow velocities) under different conditions of module length and feedwater inlet temperature. Specifically, Fig. 10a and b refer to a short module (0.1 m) and inlet temperature of 30 °C and 60 °C, respectively, while Fig. 10c and d refer to a long module (1 m) for the same temperatures. As mentioned, the influence of solar radiation on productivity is particularly appreciable in the latter (especially for low Reynolds numbers, represented by the red symbols), while it becomes negligible for short module and high inlet temperature (Fig. 10b). An intermediate case is illustrated in Fig. 10a, where, despite the short module, for $Re = 5.7$, a minor productivity increase can still be noted. However, the effect of solar radiation becomes negligible at higher flow velocities.

5. Conclusions

Amid growing water scarcity and increasing energy demands, MD powered by renewable sources, such as solar energy, has emerged as a promising desalination solution. DCMD offers advantages in thermal efficiency and operational simplicity; however, it faces challenges in maximizing productivity due to temperature and salt concentration polarization. This study systematically examines the potential of distributed solar absorption to enhance DCMD productivity by exploring various configurations, feed velocities, and solar intensities, with the aim of optimizing heat and mass transfer within the system. Our findings align with key trends observed in the literature, reinforcing the broader observation that distributed heating strategies in MD can enhance performance. Furthermore, our systematic assessment provides valuable insights toward establishing a benchmark for these unconventional configurations, which remains largely unexplored.

From a practical standpoint, this research quantitatively assesses how operating and design parameters influence single-pass water recovery. Single-pass water recovery refers to the flow of product water divided by the amount of feed solution flowing into the system for any given time interval, i.e., the fraction of water recovered with respect to that entering the membrane module(s). While this parameter does not necessarily correlate with the thermal energy consumption – particularly in systems powered entirely by solar energy – it directly affects the electrical energy required to pump water through the membrane channels, as closed-loop feed water recirculation may be needed to achieve the target system recovery rate if the value of single-pass recovery is low. The productivity results obtained in this study can be utilized to evaluate the effects of key parameters – such as feed flow velocity, channel height, feed temperature, and solar radiation – on single-pass water recovery. Generally, at a constant feed flow rate, higher water flux results in higher recovery values. Consequently, increasing feed temperature and solar radiation consistently leads to improved recovery. However, variations in flow velocities and channel heights influence both productivity and feed flow rate, complicating a straightforward assessment of their impact on single-pass water recovery. This highlights the need for a nuanced analysis of these parameters to fully understand their contributions to system performance.

Regarding scalability, further research is needed to address the integration of these modules into larger-scale systems. For example, connecting modules in series can enhance the overall temperature lift and water recovery, while parallel configurations can increase the total water production to meet higher demands. These strategies, along with the improved insulation and material selection to minimize heat losses, are crucial for the effective scale-up of solar-powered DCMD systems. Ultimately, a system-level design that optimizes both series and parallel module integration will be essential to fully exploit the benefits of direct solar absorption in large-scale desalination applications.

Overall, this work underscores the potential of distributed solar absorption to enhance DCMD productivity in a substantial manner. Solar-powered DCMD systems offer a scalable and energy-efficient approach to desalination, particularly suited for remote or off-grid applications. These insights contribute to optimizing MD system design, balancing heat transfer, and minimizing salt accumulation while providing robust productivity metrics essential for the advancement of solar-driven desalination technologies.

Declaration of competing interest

The authors declare that they have no known competing financial interests or personal relationships that could have appeared to influence the work reported in this paper.

Acknowledgments

This work was funded by the European Union Horizon Europe Research and Innovation Programme under grant agreement number 101091915 (acronym “MEloDIZER”). Views and opinions expressed are however those of the author(s) only and do not necessarily reflect those of the European Union or the European Health and Digital Executive Agency (HADEA). Neither the European Union nor the granting authority can be held responsible for them. M.M., M.F. and A.T. thank the CleanWaterCenter@PoliTo.

Appendix A. Supplementary data

Supplementary data to this article can be found online at https://doi.org/10.1016/j.desal.2025.118740.

Data availability

Research Link Provided

Dataset for "Systematic exploration of direct solar absorption potential to enhance direct contact membrane distillation" (1.0) (Original data) (ZENODO)

References

[1] World Water Assessment Programme, The United Nations World Water Development Report, 2016.
[2] S. Kumar, M. Kumar, S. Chowdhury, B. Rajpurohit, J. Randhawa, Environmental concerns and long-term solutions for solar-powered water desalination, J. Clean. Prod. 131180 (2022).
[3] H. Sharon, K. Reddy, A review of solar energy driven desalination technologies, Renew. Sust. Energ. Rev. 41 (2015) 1080–1118, https://doi.org/10.1016/j.rser.2014.09.002.
[4] J. Bundschuh, M. Kaczmarczyk, N. Ghaffour, B. Tomaszewska, State-of-the-art of renewable energy sources used in water desalination: present and future prospects, Desalination 508 (2021) 115035, https://doi.org/10.1016/j.desal.2021.115035.
[5] W. He, G. Huang, C. Markides, Synergies and potential of hybrid solar photovoltaic-thermal desalination technologies, Desalination 552 (2023) 116424.
[6] M. Morciano, M. Malaguti, F. Ricceri, A. Tiraferri, M. Fasano, Process optimization of osmotic membrane distillation for the extraction of valuable resources from water streams, npj Clean Water 7 (1) (2024) 1.
[7] S. Hota, S. Hada, C. Keske, G. Diaz, Feasibility of desalination by solar stills for small community scale freshwater demand, J. Clean. Prod. 134595 (2022).
[8] R. Deng, L. Xie, H. Lin, J. Liu, W. Han, Integration of thermal energy and seawater desalination, Energy 35 (2010) 4368–4374, https://doi.org/10.1016/j.energy.2009.05.025.

[9] L. Eykens, K. De Sitter, C. Dotremont, L. Pinoy, B. Van der Bruggen, Membrane synthesis for membrane distillation: a review, Sep. Purif. Technol. 182 (2017) 36–51, https://doi.org/10.1016/j.seppur.2017.03.035.

[10] A.N. Tabasian, F. Ricceri, M. Morciano, G. Boscheri, R. Perelli, M. Fasano, A. Tiraferri, Modeling and experimental evaluation of membrane distillation aimed at urine treatment for direct potable reuse in space stations, Desalination 572 (2024) 117119.

[11] E.T. Sayed, A. Olabi, K. Elsaid, M. Al Radi, C. Semeraro, M.H. Doranehgard, M. E. Eltayeb, M.A. Abdelkareem, Application of artificial intelligence techniques for modeling, optimizing, and controlling desalination systems powered by renewable energy resources, J. Clean. Prod. 413 (2023) 137486.

[12] S. Kalla, K. Piash, O. Sanyal, Anti-fouling and anti-wetting membranes for membrane distillation, J. Water Process Eng. 46 (2022) 102634, https://doi.org/10.1016/j.jwpe.2022.102634.

[13] Y. Suga, R. Takagi, H. Matsuyama, Effect of hollow fiber membrane properties and operating conditions on preventing scale precipitation in seawater desalination with vacuum membrane distillation, Desalination 527 (2022) 115578, https://doi.org/10.1016/j.desal.2022.115578.

[14] E. Ali, J. Orfi, H. AlAnsary, S. Soukane, H. Elcik, A. Alpatova, N. Ghaffour, Cost analysis of multiple effect evaporation and membrane distillation hybrid desalination system, Desalination 517 (2021) 115258, https://doi.org/10.1016/j.desal.2021.115258.

[15] N. Ghaffour, J. Bundschuh, H. Mahmoudi, M. Goosen, Renewable energy-driven desalination technologies: a comprehensive review on challenges and potential applications of integrated systems, Desalination 356 (2015) 94–114, https://doi.org/10.1016/j.desal.2014.10.024.

[16] M. Giagnorio, M. Morciano, W. Zhang, C. Hélix-Nielsen, M. Fasano, A. Tiraferri, Coupling of forward osmosis with desalination technologies: system-scale analysis at the water-energy nexus, Desalination 543 (2022) 116083.

[17] A. Alkhudhiri, N. Darwish, N. Hilal, Membrane distillation: a comprehensive review, Desalination 287 (2012) 2–18, https://doi.org/10.1016/j.desal.2011.08.027.

[18] J. Huang, Y. Hu, Y. Bai, Y. He, J. Zhu, Solar membrane distillation enhancement through thermal concentration, Energy 211 (2020) 118720, https://doi.org/10.1016/j.energy.2020.118720.

[19] J. Zhou, F. Wang, N. Noor, X. Zhang, An experimental study on liquid regeneration process of a liquid desiccant air conditioning system (LDACS) based on vacuum membrane distillation, Energy 194 (2020) 116891, https://doi.org/10.1016/j.energy.2019.116891.

[20] E. Ang, Y. Tan, J. Chew, A three-dimensional plasmonic spacer enables highly efficient solar-enhanced membrane distillation of seawater, J. Mater. Chem. A 7 (2019) 10206–10211, https://doi.org/10.1039/C8TA11896E.

[21] S. Shalaby, F.A. Hammad, M.E. Zayed, Current progress in integrated solar desalination systems: prospects from coupling configurations to energy conversion and desalination processes, Process. Saf. Environ. Prot. 178 (2023) 494–510, https://doi.org/10.1016/j.psep.2023.08.058.

[22] P. Hogan, Sudjito, A. Fane, G. Morrison, Desalination by solar heated membrane distillation, Desalination 81 (1991) 81–90, https://doi.org/10.1016/0011-9164(91)85047-X.

[23] J. Koschikowski, M. Wieghaus, M. Rommel, Solar thermal-driven desalination plants based on membrane distillation, Desalination 156 (2003) 295–304, https://doi.org/10.1016/S0011-9164(03)00360-6.

[24] F. Banat, N. Jwaied, M. Rommel, J. Koschikowski, M. Wieghaus, Desalination by a "compact smades" autonomous solar-powered membrane distillation unit, Desalination 217 (2007) 29–37, https://doi.org/10.1016/j.desal.2006.11.028.

[25] K. Zarzoum, K. Zhani, H. Ben Bacha, J. Koschikowski, Experimental parametric study of membrane distillation unit using solar energy, Sol. Energy 188 (2019) 1274–1282, https://doi.org/10.1016/j.solener.2019.07.025.

[26] Y. Wang, Z. Xu, N. Lior, H. Zeng, An experimental study of solar thermal vacuum membrane distillation desalination, Desalin. Water Treat. 53 (2015) 887–897, https://doi.org/10.1080/19443994.2014.927187.

[27] H. Deng, et al., Modeling and optimization of solar thermal-photovoltaic vacuum membrane distillation system by response surface methodology, Sol. Energy 195 (2020) 230–238, https://doi.org/10.1016/j.solener.2019.11.006.

[28] A. Shafieian, M. Khiadani, A novel solar-driven direct contact membrane-based water desalination system, Energy Convers. Manag. 199 (2019) 112055, https://doi.org/10.1016/j.enconman.2019.112055.

[29] E. Guillen-Burrieza, et al., Experimental analysis of an air gap membrane distillation solar desalination pilot system, J. Membr. Sci. 379 (2011) 386–396, https://doi.org/10.1016/j.memsci.2011.06.009.

[30] M. Inkawhich, J. Shingler, R.S. Ketchum, W. Pan, R.A. Norwood, K. L. Hickenbottom, Temporal performance indicators for an integrated pilot-scale membrane distillation-concentrated solar power/photovoltaic system, Appl. Energy 349 (2023) 121675.

[31] H.A.L. Ouali, M.I. Soomro, S. Touili, A.A. Merrouni, Assessment of direct contact membrane distillation system driven by parabolic trough collector plant technology for electricity and freshwater production: feasibility and benchmark under different moroccan climates, Sustain. Mater. Technol. 39 (2024) e00818.

[32] K. Rahaoui, et al., Sustainable membrane distillation coupled with solar pond, Energy Procedia 110 (2017) 414–419, https://doi.org/10.1016/j.egypro.2017.03.162.

[33] Q. Ma, Z. Xu, R. Wang, Distributed solar desalination by membrane distillation: current status and future perspectives, Water Res. 198 (2021) 117154, https://doi.org/10.1016/j.watres.2021.117154.

[34] P.D. Dongare, A. Alabastri, S. Pedersen, K.R. Zodrow, N.J. Hogan, O. Neumann, J. Wu, T. Wang, A. Deshmukh, M. Elimelech, Q. Li, P. Nordlander, N.J. Halas, Nanophotonics-enabled solar membrane distillation for off-grid water purification, Proc. Natl. Acad. Sci. USA 114 (2017) 6936–6941, https://doi.org/10.1073/pnas.1701835114.

[35] G. Stincone, R.R. Meo, E. Chiavazzo, P. Asinari, M. Fasano, M. Morciano, Optimizing the marangoni effect towards enhanced salt rejection in thermal passive desalination, Desalination 583 (2024) 117673.

[36] I.A. Said, T.R. Chomiak, Z. He, Q. Li, Low-cost high-efficiency solar membrane distillation for treatment of oil produced waters, Sep. Purif. Technol. 250 (2020) 117170, https://doi.org/10.1016/j.seppur.2020.117170.

[37] Q. Li, A.J. Charlton, A. Omar, B. Dang, P. Le-Clech, J. Scott, R.A. Taylor, A novel concentrated solar membrane-distillation for water purification in a building integrated design, Desalination 535 (2022) 115828, https://doi.org/10.1016/j.desal.2022.115828.

[38] G. Antonetto, M. Morciano, M. Alberghini, G. Malgaroli, A. Ciocia, L. Bergamasco, F. Spertino, M. Fasano, Synergistic freshwater and electricity production using passive membrane distillation and waste heat recovered from camouflaged photovoltaic modules, J. Clean. Prod. 318 (2021) 128464, https://doi.org/10.1016/j.jclepro.2021.128464.

[39] S. Liang, H. Zheng, X. Ma, F. Liu, G. Wang, Z. Zhao, Study on a passive concentrating photovoltaic-membrane distillation integrated system, Energy Convers. Manag. 242 (2021) 114332, https://doi.org/10.1016/j.enconman.2021.114332.

[40] P. Dongare, A. Alabastri, O. Neumann, P. Nordlander, N. Halas, Solar thermal desalination as a nonlinear optical process, Proc. Natl. Acad. Sci. 116 (2019) 13182–13187, https://doi.org/10.1073/pnas.1905311116.

[41] A. Bamasag, E. Almatrafi, T. Alqahtani, P. Phelan, M. Ullah, M. Mustakeem, M. Obaid, N. Ghaffour, Recent advances and future prospects in direct solar desalination systems using membrane distillation technology, J. Clean. Prod. 385 (2023) 135737, https://doi.org/10.1016/j.jclepro.2022.135737.

[42] K.S.S. Christie, T. Horseman, S. Lin, Energy efficiency of membrane distillation: simplified analysis, heat recovery, and the use of waste-heat, Environ. Int. 138 (2020) 105588, https://doi.org/10.1016/j.envint.2020.105588.

[43] R.R. Meo, M. Morciano, Investigating the potentials and limitations of capillary-fed vapor generators: a heat and mass transfer study, Int. Commun. Heat Mass Transf. 137 (2022) 106309, https://doi.org/10.1016/j.icheatmasstransfer.2022.106309.

[44] E. Chiavazzo, M. Morciano, F. Viglino, M. Fasano, P. Asinari, Passive solar high-yield seawater desalination by modular and low-cost distillation, Nat. Sustain. 1 (2018), https://doi.org/10.1038/s41893-018-0186-x.

[45] R.R. Meo, M. Provenzano, M. Morciano, Investigating the solute concentration in capillary-fed vapor generators: a heat and mass transfer study, Int. Commun. Heat Mass Transf. 148 (2023) 106998.

[46] H.U.E. Hani, R. Haq, W. Liu, A. Alhushaybari, FEM based simulation for heat and fluid flow between corrugated walls with parabolic inlet velocity for high resolution results, Appl. Therm. Eng. (2024) 124340, https://doi.org/10.1016/j.applthermaleng.2024.124340.

[47] M.Y. Rachedi, D. Bechki, Y. Marif, S. Boughali, H. Bouguettaia, A novel model for optimizing tilts of four reflectors on a flat plate thermal collector: case study in Ouargla region, Case Stud. Ther. Eng. 32 (2022) 101872.

[48] A.R. Jensen, I. Sifnaios, G.P. Caringal, S. Furbo, J. Dragsted, Thermal performance assessment of the world's first solar thermal fresnel lens collector field, Sol. Energy 237 (2022) 447–455.

[49] H.J. Hwang, K. He, S. Gray, J. Zhang, I.S. Moon, Direct contact membrane distillation (DCMD): experimental study on the commercial PTFE membrane and modeling, J. Membr. Sci. 371 (1–2) (2011) 90–98.